CILAMCE
PANACM
RIO DE JANEIRO 2021

Mesh construction and computational analysis of the biomechanics of an endovascular intervention in cerebral aneurysms using Kirchhoff–Love shells

Nicolás Muzi[1,2], Francesco Camussoni[3], Luis G. Moyano[1,3,4], Daniel Millán[1,2,*]

[1]*National Scientific and Technical Research Council (CONICET)*
C1425FQB, Autonomous City of Buenos Aires (CABA), Buenos Aires, Argentina
[2]*School of Industry-Applied Sciences, National University of Cuyo*
5600, San Rafael, Mendoza, Argentina.
[3]*Balseiro Institute, National University of Cuyo.*
8400, San Carlos de Bariloche, Río Negro, Argentina.
[4]*Interdisciplinary and Statistics Physics Group, Bariloche Atomic Center, CNEA*
8400, San Carlos de Bariloche, Río Negro, Argentina.
$*$ Corresponding author: dmillan@mendoza-conicet.gob.ar

Abstract.

The mechanism of aneurysm rupture is still not fully understood. The rupture risk of the intervention may increase during endovascular occlusions of cerebral aneurysms due to a localized load in the parent vessel close to the neck, a common day-to-day situation. As a first attempt on the road towards developing a plausible analysis capable of dealing with many cases in a statistical sense, we describe the deformation kinematics using a geometrically nonlinear thin shell model under Kirchhoff-Love's assumptions in conjunction with a simplistic Kirchhoff-St. Venant's hyperelastic material model. Though it cannot assess the artery's complexity, this more straightforward yet not trivial approach enable us to statistically study the application of a concentrated load in many locations, which mimics the action of an instrument during the endovascular treatment. We performed numerical simulations on 34 cases from the AneuriskWeb Database. We present preliminary results considering a smoothly varying thickness between the parent vessel and the aneurysm dome, focusing in the mesh construction process and loading.

Keywords: Intracranial aneurysms, Cerebral artery biomechanics, Computational mechanics, Mesh surface processing

1 Introduction

At present, when an unruptured intracranial aneurysm (UIA) is diagnosed, the most common response is its treatment. However, endovascular treatments and microsurgical interventions show a non-negligible morbidity (5%-7%) and mortality (1%-2%) risk [1]. Indeed, UIAs are relatively common, with an estimated prevalence of up to 6% [2, 3], and given that many of them never break (only 1/3 in a life-long follow-up cohort [1]), physicians frequently find themselves in the dichotomy of treating or not [4]. Particularly, in addition to hemodynamic, quemo-mechanical, and morphological factors associated to the rupture risk of saccular aneurysms [5–8], the risk increases during endovascular intervention due to the external force applied by the instruments used by the professionals near the aneurysm neck, creating stress concentration on the aneurysm dome. The study of this issue is challenging due to the need of modeling the arterial wall's biomechanics, which offers a complex multi-layered structure of composite materials, each one with different mechanical behavior [9, 10]. Furthermore, the aneurysm wall exhibits several variations in its structure and mechanical behavior [11–14]. Therefore, the wall is more fragile due to these structural changes at the aneurysm dome and the transition region (on the aneurysm neck).

It is possible to find impressive technical improvements in modeling the biomechanics of blood vessels. For example, by considering incompressible nonlinear material models such as Mooney-Rivlin solid, multi-layered materials, or even incorporating fiber orientations [15, 16]. Unfortunately, these works consider either simple theoretical geometries (dome = sphere, vessel = cylinder) or a few number of cases. Furthermore, the lack of a systematic study in a statistically relevant population is noteworthy either due to the model's high resource demand or the impossibility of specifying the overall set of parameters to perform patient-specific simulations or both. On the road towards developing a plausible analysis capable of dealing with many cases in a statistical sense, we describe the deformation kinematics using a geometrically non-linear thin shell model under Kirchhoff-Love's assumptions in conjunction with a simpler Kirchhoff-St. Venant's hyperelastic material model. Though these assumptions cannot assess the artery's complexity, they allow us to study the application of a localized load in many locations and on a myriad of aneurysm cases (further details in Section 2.1). Also, as a proof of concept, we consider a larger thickness in the artery relative to the aneurysm dome as well as different Young modulus in both regions to mimic the nonuniformity of the real problem.

The present work is organized as follows. Section 2 describes the database used for this study and a brief description of the nonlinear thin shell model, the applied force model, the numerical implementation and the consideration of varying thickness. Section 3 explains the treatment of the geometrical models acquired from the database to obtain the needed meshes for the simulation. In Section 4 we analyze the results of experiments across four selected cases. Finally, we collect some conclusions in Section 5.

2 Matherials and Methods

Section 2.1 describes the AneuriskWeb database used to retrieve the aneurysm geometrical models. Section 2.2 presents a brief description of the geometrical nonlinear thin shell model within the Kirchhoff-Love theory (stretching and bending). Section 2.3 details the modeling of the localized load, and 2.4 gives information about the numerical implementation and the thickness value as function of the geodesic distance to the neck.

2.1 AneuriskWeb Database

The consulted database is a compilation of medical images and aneurysms data retrieved from the Aneurisk project between 2005 and 2008, funded by SIEMENS Medical Solutions in collaboration with several medical institutions, and carried out in the Laboratory for Modeling and Scientific Computing (MOX), Department of Mathematics at Politecnico di Milano [17]. The database contains 103 geometrical models (triangular meshes) of intracranial aneurysms of 99 different patients, retrieved from 3D rotational angiograms (23 available in the database) with an isotropic spacial resolution of 0.3 mm (256 x 256 x 256) and segmentated through a semi-automated process validated by an expert. These cases also include the ostium (polygon describing the neck), the parent vessel's centerlines and some geometrical parameters of the aneurysms such as location, classification (lateral or terminal), and rupture status (Figure 1). We examined the 46 cases located in the Internal Carotid Artery (ICA) and discarded those presenting fusiform aneurysms or saccular aneurysms with two or more domes, resulting in 40 final subjects.

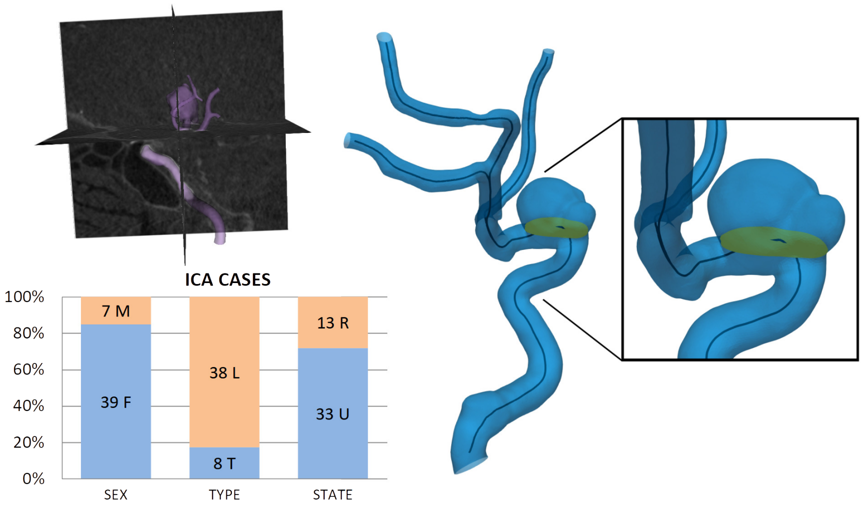

Figure 1. Left: Characteristics of the database, corresponding to the Internal Carotid Artery (ICA) cases. Type: L = lateral, T = terminal. State: R = ruptured, U = unruptured. Right: Geometrical model describing the lumen, centerlines, and the polygon describing the neck (ostium).

2.2 Geometrically non-linear thin shells elastic model

In this section, we concisely describe the mechanics of thin shells, based on a geometrically exact formulation [18]. We restrict our attention to the Kirchhoff–Love theory of shells, i.e. we neglect the shearing and stretching deformation normal to the shell mid-surface. In this theory, the shell director remains normal to the mid-surface during the deformation, see [19] and references therein.

We assume that this body can be described by the pair ($\boldsymbol{\varphi}$,$\boldsymbol{t}$), where the mapping $\boldsymbol{\varphi}$ defines the middle surface Ω of the shell, and $\boldsymbol{t}$ is a field of unitary vectors (director field). We assume a varying thickness h, and also that the change in shell thickness after the deformation is negligible. The subscript 0 indicates quantities in the reference configuration; for example, $\boldsymbol{\varphi}_0$ parameterize the reference middle surface.We follow the usual convention for Latin and Greek indices (i.e. $i = 1, 2, 3$; $\alpha = 1, 2$), a comma denotes partial differentiation, subscripts refer to covariant components, and superscripts denote contravariant components.

Then, the thin shell body $\mathscr{S}$ is given by

$$\mathscr{S} = \left\{ \boldsymbol{\Phi} \in \mathbb{R}^3 |\ \boldsymbol{\Phi} = \boldsymbol{\varphi}(\xi^\alpha) + \xi\, \boldsymbol{t}(\xi^\alpha),\ -\frac{h(\xi^\alpha)}{2} \leq \xi \leq \frac{h(\xi^\alpha)}{2},\ (\xi^1, \xi^2) \in \mathscr{A} \right\}, \tag{1}$$

where $\mathscr{A} \subset \mathbb{R}^2$ is the parametric space for the middle surface. Hence, we view a configuration $\boldsymbol{\Phi}$ as a mapping from a parametric domain $\mathscr{A} \times [-h/2, h/2]$ into $\mathbb{R}^3$. The parametric domain is described by the coordinates $\{\xi^1, \xi^2, \xi^3\}$ (where we identify $\xi = \xi^3$), whose corresponding dual basis is $\{\boldsymbol{E}^i\}$.

The area element of the deformed middle surface can be computed as $d\Omega = \bar{j} d\xi^1 \xi^2$, where $\bar{j} = \|\boldsymbol{\varphi}_{,1} \times \boldsymbol{\varphi}_{,2}\|$, and the unit normal is $\boldsymbol{t} = (\boldsymbol{\varphi}_{,1} \times \boldsymbol{\varphi}_{,2})/\bar{j}$. The membrane strain tensor is defined as $\varepsilon_{\alpha\beta} = \frac{1}{2}(\boldsymbol{\varphi}_{,\alpha} \cdot \boldsymbol{\varphi}_{,\beta} - \boldsymbol{\varphi}_{0,\alpha} \cdot \boldsymbol{\varphi}_{0,\beta})$ which measures changes in the in-plane metric tensor. The bending strain tensor, measuring changes in the second fundamental form, is given by $\rho_{\alpha\beta} = \boldsymbol{\varphi}_{,\alpha} \cdot \boldsymbol{t}_{,\beta} - \boldsymbol{\varphi}_{0,\alpha} \cdot \boldsymbol{t}_{0,\beta}$. Also, strain is expressed in terms of the kinematics of the middle surface. For an elastic lamina the potential energy is expressed exclusively in terms of the kinematics of the middle surface, that is the mapping $\boldsymbol{\varphi}$, and is written in the parametric space as

$$\Pi_{\text{tot}}[\boldsymbol{\varphi}] = \Pi_{\text{int}}[\boldsymbol{\varphi}] - \Pi_{\text{ext}}[\boldsymbol{\varphi}] = \int_{\mathscr{A}} W(\boldsymbol{\varepsilon}, \boldsymbol{\rho})\ \bar{j}_0 d\mathscr{A} + \int_{\mathscr{A}} \boldsymbol{q} \cdot (\boldsymbol{\varphi} - \boldsymbol{\varphi}_0)\ \bar{j}_0 d\mathscr{A}, \tag{2}$$

where W is the strain energy density per surface unit, and $\boldsymbol{q}$ is the external body load per unit area. Here we consider an isotropic Kirchhoff-St. Venant model as the elastic material model.

2.3 Localized force

The effect of a localized force is modeled by a Plateau function, which decays as a function of the geodesic distance on the middle surface reference configuration to the application point. This function is given as

$$\hat{q}(r) = \frac{\hat{C}}{2\pi\sigma^2} \frac{\exp\left[-\frac{1}{4}\left(\frac{r}{\sigma}\right)^4\right]}{1 + \exp\left[-\frac{1}{4}\left(\frac{r}{\sigma}\right)^4\right]}, \tag{3}$$

where r is the radial distance on a circular infinite region, σ is a given parameter that controls the function width and $\hat{C}$ is a constant computed such that the integral of $\hat{q}(r)$ equals one.

2.4 Numerical implementation

For the calculation of the total energy, it is required to obtain the second order derivatives for the deformations of the shell $\boldsymbol{\varphi}$, needing an approximation with C^1 continuity in order to use a straightforward Galerkin discretization approach. Due to this we use subdivision surfaces finite elements [20], to approximate $\boldsymbol{\varphi}$. A Lagrangian approach was followed, with the same space of basis functions for both the deformed and the reference configurations. Being $\boldsymbol{\varphi}_0$ the mapping of the reference configuration

$$\boldsymbol{\varphi}_{0h}(\xi^1, \xi^2) = \sum_{a=1}^{N} B_a(\xi^1, \xi^2) \boldsymbol{\varphi}_{0a}, \tag{4}$$

where $B_a(\xi^1, \xi^2)$ are subdivision surfaces basic functions, N the number of nodes in the mesh, and $\boldsymbol{\varphi}_{0a}$ the position in the tridimensional space of the a-th control point defining the middle surface of the undeformed shell.

It is noteworthy that it is possible to make use of a prescribed shell thickness, discretized as follows

$$h_h(\xi^1, \xi^2) = \sum_{a=1}^{N} B_a(\xi^1, \xi^2) h_a, \tag{5}$$

where h_a are predefined values of the shell thickness at the reference nodes. It is known that in the aneurysm neck, the thickness decreases dramatically. Still, this transition hasn't been defined with certainty [14, 21]. We can assume that the thickness of the shell varies according to the arctangent of the geodesic distance on the aneurysm from the node to the neck curve. The function used to assign a thickness value for each node is

$$h_a = (\bar{h}_v - \bar{h}_d)\frac{1}{\pi}\left(\tan^{-1}\frac{d_{Ga}}{w} + \frac{\pi}{2}\right) + \bar{h}_d, \tag{6}$$

where $\bar{h}_v$ and $\bar{h}_d$ are the values of the thickness in the blood vessel and the dome (reported values), w is the width of the transition zone, and d_{Ga} the value of the geodesic distance between the a-th node and the curve defining the aneurysm neck. This geodesic distance is calculated by the CGAL library [22]. We provide further information about it in Section 3.

When using the load function given by Equation (3) for a curved surface the distance r is replaced by the geodesic distance d_G, while the load is $\boldsymbol{q} = Q\,\hat{q}(d_G)\,\boldsymbol{t}_0$, where Q is the load value (100 mmHg), whereas $\sigma = 0.25$ mm, emulating the diameter of a microcatheter of 1.5 Fr (0.5 mm), and $\hat{C}$ is computed such that the integral of $\hat{q}(d_G)$ on the middle surface Ω_0 equals one. The total energy function is expressed in terms of the nodal variables $\boldsymbol{\varphi}_a$, $a = 1, 2, \ldots, N$, which is minimized with respect to the degrees of freedom given by the deformation using the Newton-Raphson method, combined with a linear search method [19]. This is repeated until the convergence criterion is reached, then the next load site is selected and the whole process is repeated.

3 Surfaces mesh treatment

Our study focuses on the region surrounding the aneurysm neck. As shown in Figure 1, models acquired from the database included a mesh describing the blood vessel tree containing the aneurysm and poor mesh quality in regions with high curvature. Therefore, to perform efficient numerical simulations, a pre-process was needed to obtain the final meshes, as described in Figure 2, left. From 40 initial cases, 34 final meshes were obtained, as 6 cases presented issues at some step of the process. For this purpose, we developed a C++ computational framework that enables us to combine VTK (Visualization Toolkit, [23]) and CGAL libraries for mesh processing.

3.1 Aneurysm isolation

As a first step, we isolated each aneurysm dome from its parent vessel by cutting at a certain distance from the neck, discarding the rest of the artery. The procedure is carried out in a semi-automated fashion by an application developed in C++ and using the VTK library, such that the user defines the distance as a multiple of the vessel's inner diameter on each side of the neck (Figure 2, center). According to the database classification, the algorithm inputs are the geometrical model, the neck polygon, the centerlines, the selected distance (as a multiple of the diameter), and a variable indicating if the aneurysm is terminal or lateral. Then, for each model, it picks reference points on each centerline, measures the inner diameter of each vessel at the neck area, and moves along the parent vessel, performing the clip at the desired distance.

We perform the cut by defining a cylinder oriented perpendicularly to the centerline in the selected point. After the clip the arterial tree is discarded, keeping only the connected component associated with the model neck. In this work, we set up the isolation at a distance of 2.5 times the vessel diameter, based on analyzing the problem's behavior to different lengths. Higher values (>3 times the diameter) presented more stability but caused a flexion effect on the model and an excessive dome movement. This isolation algorithm successfully performed ∼89% of the overall cuts, while the rest had to be executed manually by a trained user. Each manual isolation required between 10-20 minutes per case depending on the model complexity, while the automated isolation spent 3-4 seconds.

After the isolation we applied a remeshing step [22], maintaining the original element edge size of 0.25 mm. Due to the impact of the neck in steps 4 and 5, (Figure 2, left), we refined the neck area through the isotropic remeshing algorithm from CGAL's "*Polygon Mesh Processing*" library [22]. We apply a final iteration of the Loop's subdivision surface scheme, see Figure 2, right, generating edges of 0.0625 mm in length for the refined region around the neck and 0.125 mm for the rest of the model.

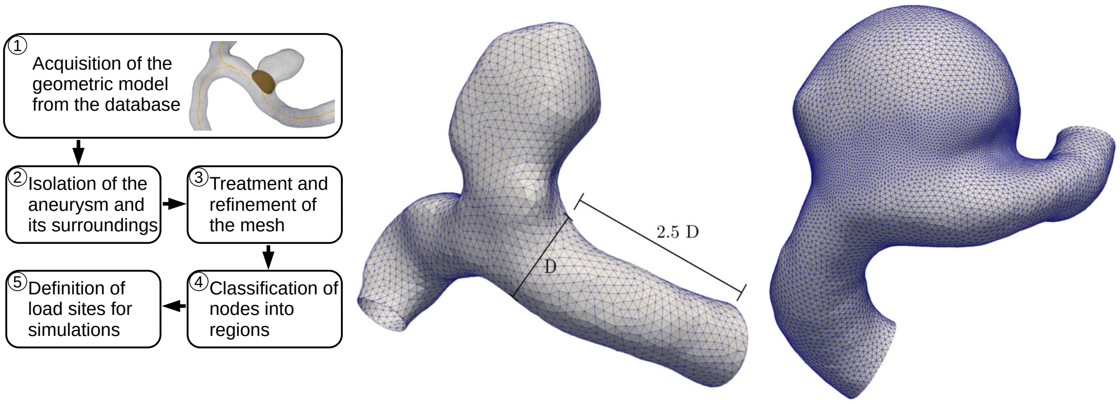

Figure 2. Left: Mesh processing steps. Center: Example of an isolated model (C0005). Right: Example of a remeshed model, with refined neck (C0034).

3.2 Geodesic distance

We developed an algorithm that finds the geodesic position of each node to the ostium and assigns a "tag" to it, to distinguish between dome and artery nodes. In this step, we also used algorithms described in the section *Triangulated Surface Mesh Shortest Paths* of the CGAL library [22]. This library computes geodesic paths on a triangulated surface mesh. We calculated the geodesic distance between each node and the neck curve (Figure 3, left) and assigned it a positive sign if the node was located on the aneurysm or a negative if it was located on the dome (Figure 3, right). The final step consisted on the definition of a region surrounding the artery in the neck area. This loading zone (or "vest") was defined at a distance of 1 time the vessel's inner diameter, similarly to the isolation step but only applied to artery nodes (Figure 3, right). In this region we considered a distribution of loading points (Figure 3, right), each of which are used to simulate the effect of a tool pressing in that position during endovascular occlusion intervention. These load sites were selected so as the minimum distance between them is 0.5 mm, keeping the density as regular as possible. The applied load corresponds to the function described in Section 2.

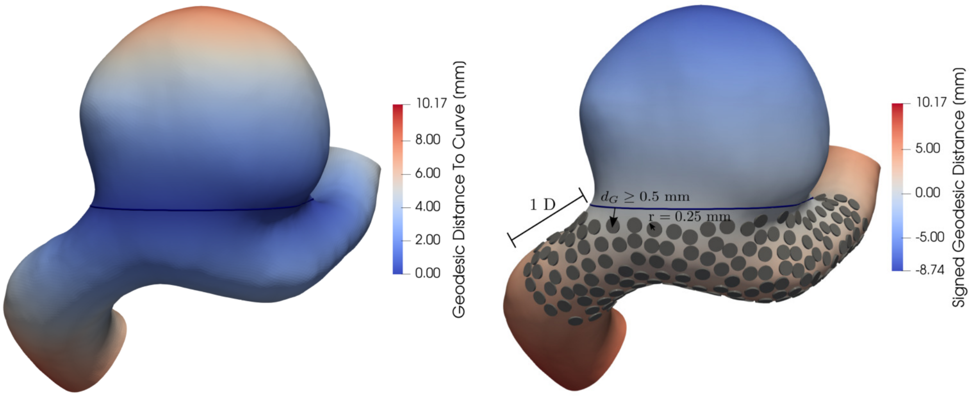

Figure 3. Case C0034. Left: geodesic distance to the neck curve field. Right: detail of the load sites. Each one of them has a radius r of 0.25 mm (for visualization) and are located at a minimum distance (d_G) of 0.5 mm from each other. Load sites are limited to a vest region around the neck, defined with the same algorithm that performs the isolation, at a distance of one inscripted diameter from the neck curve.

4 Experiments and results

We conducted experiments with the long-term objective of determining which areas of an aneurysm have a higher sensitivity to localized loads and could lead to rupture. Thus, we focus on the amount of deformation as an interesting first case of study. A particular case of large deformation is the presence of buckling effects, i.e. strong deformations associated with small increases in load. For this, we established which biomechanical variables are involved in large perturbations of an aneurysm when pressure is applied. For each loading point (Figure 3), an independent experiment was carried out. For the final state of the deformed mesh, a number of biomechanical observables were measured at specific points inside the mesh triangles (Gauss points) specifying a complete biomechanical model. The observables included displacement magnitudes, differences between the Gaussian curvature at the reference and the deformed configurations of the Gauss points, total energy, membrane energy, bending energy, among others. Figure 4 shows dimensionless relations between different physical variables for all loading sites belonging to four selected ICA cases (C0090, C0034, C0014, and C0042), colored by manually identifying the final state for presence (blue) or absence (orange) of buckling effects. Remarkably, the loading sites group in two quite distinct clusters with some overlap, suggesting that this visualization method is an efficient tool to capture specific aneurysm areas that lead to large deformations and are likely to be associated with ruptured states.

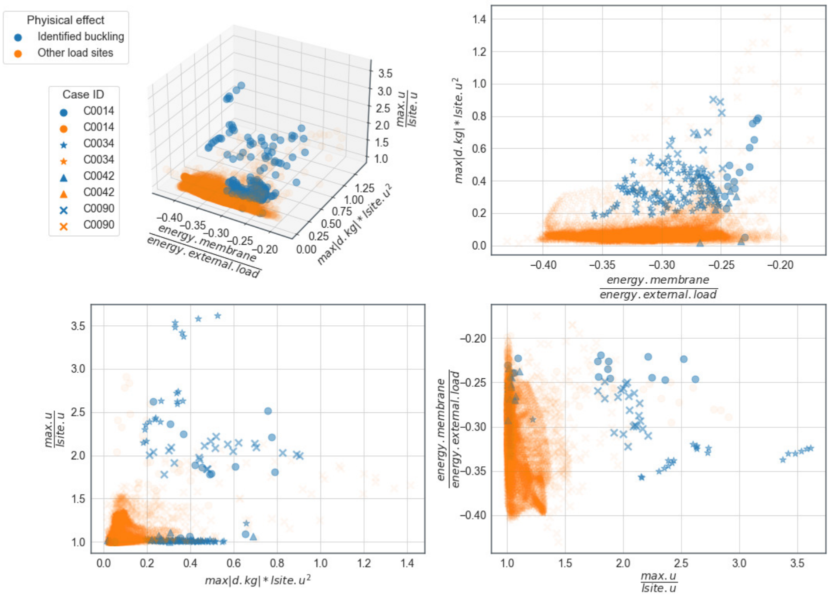

Figure 4. Top left: representation of dimensionless biomechanical atributes for all load sites of four selected ICA cases, colored by manual inspection of presence (blue) or absence (orange) of buckling effects. Remaining panels: pairwise atributes projections. For the considered combinations the loading sites group in two clusters with minimum overlap, as it can be seen in the projections. max.u = max displacement of nodes, lsite.u = displacement of the load site, max|d.kg| = max difference of gaussian curvature between reference and deformed configurations.

5 Conclusions and future directions

This work presents preliminary results of a thin shell model considering a smoothly varying thickness between the parent vessel and the aneurysm dome. We developed a semi-automated process to isolate and remesh the aneurysm dome and its neighboring connected parent vessels, allowing us to treat a large number of cases, saving time and resources. The algorithm allows the isolation of any type of aneurysm, as every measure considered for the process is relative to the dimensions of each case. Also, we show that the computational analysis of the biomechanics of intracranial aneurysms can help to determine non-trivial areas of interest for selecting case studies given wall thickness and concentration load location. In future work we plan to modify the isolation algorithm to raise its success rate, and expand the use of the database to other problems and situations, studying aneurysm biomechanics considering more complex materials such as a Mooney-Rivlin solid (ongoing work), an anisotropic multilayered structure or including other studies of interest, such as crack phase-field modeling of aneurysm rupture [24], heading towards a better rupture risk assesment.

Acknowledgements. This work was funded by the Investigation Projects PICTO-2016-0054 UNCuyo-ANPCyT, L028-2019 and M084-2019 SIIP UNCuyo.

Authorship statement. The authors hereby confirm that they are the sole liable persons responsible for the authorship of this work, and that all material that has been herein included as part of the present paper is either the property (and authorship) of the authors, or has the permission of the owners to be included here.

References

[1] A. E. Lindgren, T. Koivisto, J. Björkman, von und zu M. Fraunberg, K. Helin, J. E. Jääskeläinen, and J. Frösen. Irregular shape of intracranial aneurysm indicates rupture risk irrespective of size in a population-based cohort. *Stroke*, vol. 47, n. 5, pp. 1219–1226, 2016.

[2] J. Wardlaw and P. White. The detection and management of unruptured intracranial aneurysms. *Brain*, vol. 123, n. 2, pp. 205–221, 2000.

[3] M. H. Vlak, A. Algra, R. Brandenburg, and G. J. Rinkel. Prevalence of unruptured intracranial aneurysms, with emphasis on sex, age, comorbidity, country, and time period: a systematic review and meta-analysis. *Lancet Neuro*, vol. 10, n. 7, pp. 626–636, 2011.

[4] W. Van Rooij and M. Sluzewski. Procedural morbidity and mortality of elective coil treatment of unruptured intracranial aneurysms. *Am J Neuroradiol*, vol. 27, n. 8, pp. 1678–1680, 2006.

[5] K. Kayembe, M. Sasahara, and F. Hazama. Cerebral aneurysms and variations in the circle of willis. *Stroke*, vol. 15, n. 5, pp. 846–850, 1984.

[6] T. R. Forget Jr, R. Benitez, E. Veznedaroglu, A. Sharan, W. Mitchell, M. Silva, and R. H. Rosenwasser. A review of size and location of ruptured intracranial aneurysms. *Neurosurgery*, vol. 49, n. 6, pp. 1322–1326, 2001.

[7] V. Costalat, M. Sanchez, D. Ambard, L. Thines, N. Lonjon, F. Nicoud, H. Brunel, J. P. Lejeune, H. Dufour, P. Bouillot, and others. Biomechanical wall properties of human intracranial aneurysms resected following surgical clipping (irras project). *J Biomech*, vol. 44, n. 15, pp. 2685–2691, 2011.

[8] R. D. Millan, L. Dempere-Marco, J. M. Pozo, J. R. Cebral, and A. F. Frangi. Morphological characterization of intracranial aneurysms using 3-d moment invariants. *IEEE T Med Imaging*, vol. 26, n. 9, pp. 1270–1282, 2007.

[9] A. M. Robertson and P. N. Watton. Mechanobiology of the arterial wall. *Transport in biological media*, vol. 1, pp. 275–7, 2013.

[10] P. R. Hoskins, P. R. Hoskins, P. V. Lawford, P. V. Lawford, B. J. Doyle, and B. J. Doyle. *Cardiovascular biomechanics*. Springer, 2017.

[11] J. Humphrey and P. Canham. Structure, mechanical properties, and mechanics of intracranial saccular aneurysms. *J Elasticity*, vol. 61, n. 1, pp. 49–81, 2000.

[12] L. E. Savastano, A. Bhambri, D. A. Wilkinson, and A. S. Pandey. Biology of cerebral aneurysm formation, growth, and rupture. In *Intracranial Aneurysms*, pp. 17–32. Elsevier, 2018.

[13] J. Frösen. Smooth muscle cells and the formation, degeneration, and rupture of saccular intracranial aneurysm wall—a review of current pathophysiological knowledge. *Transl Stroke Res*, vol. 5, n. 3, pp. 347–356, 2014.

[14] R. Tulamo, J. Frösen, J. Hernesniemi, and M. Niemelä. Inflammatory changes in the aneurysm wall: a review. *J Neurointerv Surg*, vol. 10, n. Suppl 1, pp. i58–i67, 2018.

[15] P. N. Watton, Y. Ventikos, and G. A. Holzapfel. Modelling the growth and stabilization of cerebral aneurysms. *Math Med Biol*, vol. 26, n. 2, pp. 133–164, 2009.

[16] A. Selimovic, Y. Ventikos, and P. N. Watton. Modelling the evolution of cerebral aneurysms: biomechanics, mechanobiology and multiscale modelling. *Procedia IUTAM*, vol. 10, pp. 396–409, 2014.

[17] Aneurisk-Team. AneuriskWeb project website, http://ecm2.mathcs.emory.edu/aneuriskweb. Web Site, 2012.

[18] J. Simo and D. Fox. On a stress resultant geometrically exact shell model. Part I: Formulation and optimal parametrization. *Comput Method Appl M*, vol. 72, pp. 267–304, 1989.

[19] D. Millán, A. Rosolen, and M. Arroyo. Nonlinear manifold learning for meshfree finite deformation thin-shell analysis. *Int J Numer Meth Eng*, vol. 93, n. 7, pp. 685–713, 2013.

[20] F. Cirak and Q. Long. Subdivision shells with exact boundary control and non-manifold geometry. *Int J Numer Meth Eng*, vol. 88, n. 9, pp. 897–923, 2011.

[21] L. M. Kadasi, W. C. Dent, and A. M. Malek. Cerebral aneurysm wall thickness analysis using intraoperative microscopy: effect of size and gender on thin translucent regions. *J Neurointerv Surg*, vol. 5, pp. 201–206, 2013.

[22] The CGAL Project. *CGAL User and Reference Manual*. CGAL Editorial Board, 5.2.2 edition, 2021.

[23] W. Schroeder, K. Martin, and B. Lorensen. *The Visualization Toolkit*. Kitware, 2006.

[24] O. Gültekin, H. Dal, and G. Holzapfel. Crack phase-field modeling of anisotropic rupture in fibrous soft tissues. In *proceedings of the XIV COMPLAS*, pp. 139–150. CIMNE, 2017.